Engineering Transactions, **73**, https://doi.org/10.24423/engtrans.3430.2025
Institute of Fundamental Technological Research Polish Academy of Sciences (IPPT PAN)
Université de Lorraine • Poznan University of Technology

Research Paper

Enhancement of the Thermal Stability of Engine Block Alloy Al-10Si-1Cu-0.5Mg-0.5Ni-0.5Fe with Trace Additions of Ti and Zr

Mohammad Salim KAISER

Innovation Centre, International University of Business Agriculture and Technology
Dhaka-1230, Bangladesh; e-mail: dkaiser.res@iubat.edu

An investigation was carried out on the Al-10Si-1Cu-0.5Mg-0.5Ni-0.5Fe alloy engine block, emphasizing its physical and mechanical characteristics, as well as the presence of trace titanium (Ti) and zirconium (Zr). Three different alloys underwent processes such as homogenization, T6 solution treatment, quenching, and aging to observe both natural and artificial aging responses. The development of Al_2Cu and Mg_2Si phases within the aluminum matrix during the aging process led to the attainment of peak-aged strength. However, this strength diminished in the over-aged condition due to precipitation coarsening and recrystallization phenomena. The addition of Ti effectively refined the α-Al grain structure and led to the formation of thermally stable nano-sized Al_3Ti dispersoids, which did not significantly enhance strength but prevented a drastic decline in the strength of the thermally damaged alloy. The simultaneous addition of Ti and Zr to the alloy further facilitated the precipitation of $Al_3(Ti, Zr)$ dispersoids, enhancing this capability. Trace addition reduced the alloys' toughness as well as thermal conductivity to a small extent due to grain refinement and precipitation formation, but these properties improved during aging due to recovery and recrystallization. Microstructural analysis of the alloys indicated that trace additions facilitated the formation of more finely distributed grains, contributing to grain refinement and preventing recrystallization in the over-aged state. The enhanced homogeneity of the grains due to trace additions was further supported by fractography studies.

Keywords: Al-Si engine block; trace addition; age hardening; thermal conductivity; mechanical properties; microstructure.

1. INTRODUCTION

Aluminum-silicon alloys are highly regarded for their multitude advantages across various industries. These benefits include exceptional specific strength, which makes them ideal for various applications that require both durability and reduced weight. Additionally, these alloys excel in heat transfer capabilities, allowing for efficient thermal management in diverse engineering and manufacturing processes [1–3]. These advantageous characteristics position them as promising candidates to potentially replace components typically made from ferrous alloys in various applications across industries seeking enhanced performance, reduced overall weight, and improved thermal conductivity. During the manufacturing process, engine blocks, which were typically made of hypoeutectic alloys like A356 or A380, were found to exhibit a reasonable degree of wear resistance, despite featuring cast-in steel liners [1, 4]. This raised concerns within the production team about the alloys' long-term durability and performance under varying conditions. Alloying additions are incorporated into binary Al-Si alloys to enhance their specific characteristics, including mechanical properties such as yield and ultimate tensile strength, fatigue strength, corrosion resistance, and fabrication attributes like castability, formability, forgeability, and machinability [5–7].

Additions of key alloying elements commonly found in Al-Si alloys utilized in engine blocks include copper, magnesium, nickel, sodium, manganese, iron, and strontium, all of which contribute to optimal performance and durability in engine block applications [8, 9]. Among these elements, copper (Cu) and magnesium (Mg) play crucial roles as the two most significant elements added to Al-Si alloys to enhance their strength, though they occasionally reduce ductility. The addition of Cu and Mg specifically contributes to improving the strength and hardness of the alloys under various conditions, such as casting and heat treatment, with the most substantial improvements in mechanical properties [10–12]. On the other hand, the introduction of nickel (Ni) in Al-Si alloys has been shown to enhance mechanical properties at elevated temperatures while simultaneously decreasing the coefficient of thermal expansion [13, 14]. Notably, a study by Cho *et al.* [15] confirmed that the combined increase of Cu and Ni in Al-12% Si alloys had a positive effect on the mechanical properties at high temperatures.

In casting processes, iron (Fe) and manganese (Mn) are usually regarded as impurities. However, , iron reacts to form various insoluble intermetallic phases such as $FeAl_3$, $FeMnAl_6$, and α-AlFeSi, which contribute to strength improvements at higher temperatures [16, 17]. Nevertheless, an increase in Fe content due to these insoluble phases can adversely affect the casting's feeding characteristics. The incorporation of transition elements, such as Zr, into Al-Si automotive alloys plays a critical role in the formation of tri-aluminides, which are characterized by their low solubility and low diffusion coefficient [18, 19]. Their strategic addition serves as a valuable tool in regulating the microstructure of these alloys, ultimately enhancing their mechanical properties and performance. Previous studies have extensively documented that the strength of Al-Si alloys begins to diminish noticeably when the temperature surpasses approximately 200°C. This decline can be attributed to the prevalent phenomenon of precipitation coarsening, which leads to the formation of larger particles within the alloy's microstructure. Consequently, these alterations in the alloy's microstructure cause significant modifications to its mechanical properties. In essence, the gradual decline in strength observed in Al-Si alloys at elevated temperatures can be directly linked to the intricate process of precipitation coarsening, which causes pronounced modifications in the overall structural characteristics of these alloys [20, 21].

Titanium is widely recognized for its potential as a recrystallization inhibitor and grain refiner in aluminum and its alloys [22, 23]. However, there has been limited research conducted on its influence in cast Al-Si automotive alloys. The primary objective of this study is to investigate the effects of trace Ti, both individually and in combination with Zr, on various physical and mechanical properties, including hardness, thermal conductivity, tensile strength, impact resistance, fracture toughness, and microstructural characteristics of an Al-Si automotive alloy, considering the impact of aging. Consequently, the aim is to develop a novel class of alloy, denoted as Al-10Si-1Cu-0.5Mg-0.5Ni-0.5Fe-0.2Ti-0.2Zr, which is envisioned to offer enhanced versatility and performance compared to the currently available alloys on the market.

2. Experimental methods

Melting was conducted in a resistance heating furnace using the conventional method with the use of a clay-graphite crucible. Initially, a commercially used aluminum engine block was melted to serve as the master alloy. Three heats were conducted to produce Al-Si automotive alloys: one with trace Ti, and another with both Ti and Zr. The development of these alloys involved the use of 99.98% purity Ti in powder form and an Al-10%Zr master alloy. The Ti powder, enclosed in aluminum foil, was added by plunging. The final melt temperature was consistently maintained at 750 ±15°C. Casting was carried out in an adjustable mild steel metal mold, preheated to 200°C, and adjusted to a size of 20 × 100 × 200 mm. The alloy underwent analysis using a spectrochemical method, and the chemical composition is detailed in Table 1, excluding negligible elements such as Pb, Sn, P, and others.

The cast alloys underwent homogenization at 400°C in a muffle furnace for one day and were then air-cooled normally to relieve internal stresses. Subsequently, the homogenized samples were solutionized at 530°C for four hours, followed by water with salt-ice quenching to achieve a super saturated single-phase region. The solutionized alloys were then cut into pieces measuring 20 mm × 20 mm × 5 mm for the purpose of conducting natural aging for two months,

TABLE 1. Chemical composition of the three alloys expressed in weight percent.

	Si	Cu	Mg	Ni	Fe	Ti	Zr	Al
Alloy 1	10.280	1.107	0.520	0.506	0.501	0.002	0.001	Bal
Alloy 2	10.110	1.038	0.530	0.528	0.504	0.105	0.004	Bal
Alloy 3	10.210	1.009	0.513	0.532	0.514	0.102	0.120	Bal

Remarks:
Alloy 1: Al-10Si-1Cu-0.5Mg-0.5Ni-0.5Fe
Alloy 2: Al-10Si-1Cu-0.5Mg-0.5Ni-0.5Fe-0.1Ti
Alloy 3: Al-10Si-1Cu-0.5Mg-0.5Ni-0.5Fe-0.1Ti-0.1Zr

as well as artificial aging involving both isochronal and isothermal treatments at various temperatures for different durations. The age-hardening behavior was monitored through hardness measurements. A Muffle Furnace JSMF-30T was employed for all heat treatment processes. After heat treatment, the sample surfaces were polished to facilitate hardness and conductivity measurements. Micro Vickers Hardness Tester(HV-1000DT model) was utilized to evaluate the microhardness of the samples by applying a 1 Kg load for 10 s using a Knoop indenter. The electrical conductivity of the alloys was determined using an electrical conductivity meter (type 979), while thermal conductivity was calculated based on this data using the Wiedemann-Franz law [24]. A minimum of fifteen readings were taken at varying locations on each polished sample for both studies. Tensile testing was carried out on standard samples using a 4204 model Instron testing machine at a strain rate of 10^{-3} 1/s. The tensile test samples had dimensions of 25 mm gauge length, 6 mm width, and 5 mm thickness. The tests were performed at ambient temperature in accordance with ASTM standards, and the average results of five test being recorded. The true stress and true strain curve was plotted based on the value closest to the average of the experimental tensile results.

The specimens were initially polished using metallographic sandpaper, followed by a final polish with alumina. Standard Keller's reagent served as the etchant, and the specimens were etched for approximately 15 s before microstructures were observed using a trinocular inverted metallurgical microscope (Model SKU: ME1200TB-10MA). Subsequently, in-depth scanning electron microscopy (SEM) and energy dispersive X-ray (EDX) analysis were conducted on the aged specimens using the JEOL JSM-5200 scanning electron microscope, which features an energy dispersive X-ray analyzer (Model: Link AN-10000). Additionally, the scanning microscope was utilized not only for the analysis of the aged specimens but also to investigate the fracture mode of tensile-tested specimens and to examine the worn surface of alloys subjected to various wear studies.

3. Results and discussion

3.1. Aging behavior

3.1.1. Natural aging. Upon subjecting the solution-treated hypoeutectic Al-Si automotive base Alloy 1, trace Ti-added Alloy 2, and Alloy 3 with both trace Ti and Zr to natural aging for two months, the change in hardness over time was documented and is illustrated in Fig. 1. Notably, all three alloys displayed a certain degree of age hardening. It is hypothesized that as materials undergo natural aging, solute atoms combine to form clusters or co-clusters, consisting of Si, Cu, and Mg, within the matrix. These clusters are believed to impede dislocation movement, leading to an observed increase in hardness [25]. The addition of trace amounts of Ti in the alloy delayed the age hardening process. This delay is attributed to the formation of Ti tri-aluminide, which inhibits the development of clusters or co-clusters within the alloy's matrix. Conversely, the presence of Zr leads to the formation of additional Zr tri-aluminide, which enhances the alloy's properties, thereby further prolonging the time required to realize the benefits of natural aging [26, 27]. The introduction of trace elements into the alloy refines the grain structure and modifies the morphology and size of the eutectic Si phase. Initially, this leads to a decrease in hardness, followed by an increase in hardness due to grain refinement, as indicated by the Hall-Petch equation [28, 29]. All alloys exhibited a reduction in hardness after a short period of time, which is likely the result of internal stress relief caused by the casting and solution processes.

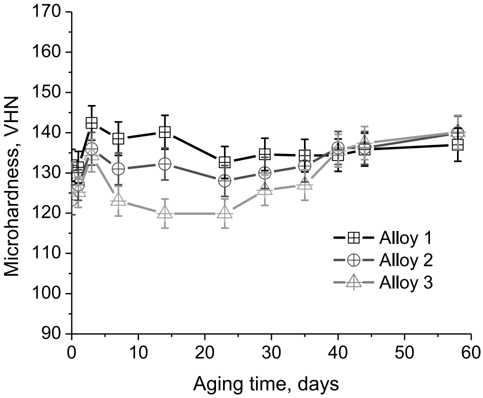

Fig. 1. Hardness change brought on by trace additions over 58 days of natural aging for the alloys.

3.1.2. Artificial aging: Isochronal aging. All three alloys underwent solution treatment followed by isochronal aging for 90 min. The variations in microhardness resulting from different aging temperatures are illustrated in Fig. 2.

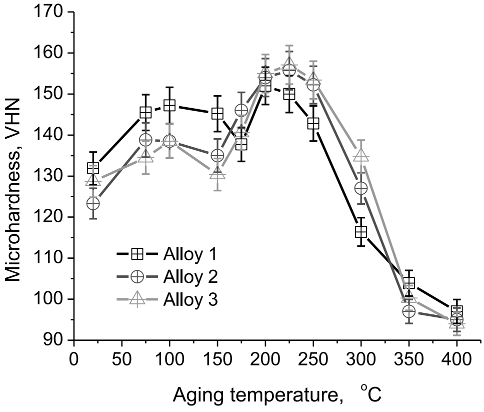

Fig. 2. Hardness curves resulting from the experimental alloys' 90-minute isochronal aging.

Notably, all three alloys exhibit a distinct pattern characterized by two aging peaks, a phenomenon previously documented by numerous researchers in the context of automotive alloys [10, 12]. Initially, the hardness increases throughout the early stages of aging until it reaches the first peak. Subsequently, a slight reduction in hardness occurs, followed by another increase that culminates in the second peak. In the final phase of aging, a pronounced decline in hardness is observed, attributed to over-aging effects. This remarkable behavior has been corroborated by various studies and exemplifies a specific precipitation sequence associated with this alloy, which includes the formation of Guinier-Preston (GP) zones, the precipitation of homogeneous θ''-Al_2Cu and β''-Mg_2Si intermetallic phases, as well as the heterogeneous precipitation of θ'-Al_2Cu and β'-Mg_2Si intermetallic phases. This ultimately leads to the formation of equilibrium phases of θ-Al_2Cu and β-Mg_2Si in rod or plate shapes. The two aging peaks are primarily influenced by the GP zone and metastable phases, respectively. The maximum strength of the alloy is achieved prior to the precipitation of the incoherent θ and β platelets.

Additionally, phases such as β-Al_5FeSi, π-$Al_9FeMg_3Si_5$, and Q-$Al_5Cu_2Mg_8Si_6$ may form, although each contributes less to the overall strength compared to the θ and β phases. The alloy also exhibits the formation of ε-Al_3Ni, δ-Al_3CuNi and T-Al_9FeNi phases due to the presence of Ni, contributing to the high thermal stability of the material [30]. During the initial stages of aging, a uniform distribution of fine and abundant GP zones within the matrix results in a significant increase in strength. Subsequently, in the intermediate aging phase, metastable phases develop and remain semi-coherent with the matrix, effectively impeding dislocation movement and providing additional strengthening [11]. The dissolution of GP zones becomes prominent as the alloy transitions to metastable phases, leading to a notable decrease in their number. However, the small size of metastable precipitates limits their ability to effectively resist dislocation movement, resulting in a reduction in the age-hardening effect between the two aging peaks. The softening of the alloy at higher temperatures may be attributed to particle coarsening and recrystallization effects.

Alloys containing trace additives demonstrate increased strength when exposed to elevated aging temperatures. The introduction of trace amounts of Ti into the alloy results in the formation of the $L1_2$-ordered Al_3Ti phase during both melting and heat treatment. These coherent and thermally stable Al_3Ti particles, with higher melting points compared to the Al matrix, act as strong barriers to dislocation movement, effectively pinning grain and sub-grain boundaries during various thermal processing steps of aluminum alloys. Furthermore, the addition of Zr leads to the formation of the $Al_3(Ti, Zr)$ phase, further enhancing the properties of the alloy [31, 32]. In addition to the intermetallic formation findings reported in the TEM study by other researchers, it is important to note that this finding encompasses various types of Al-alloys beyond the binary ones. The comprehensive insights gained from these studies provide a better understanding of the intricate processes involved in the development of intermetallic compounds in aluminum systems [27, 33, 34].

The thermal conductivity changes of all three experimental alloys are presented in Fig. 3, illustrating their evolution during isochronal aging under identical conditions. The similarity in the nature of the conductivity curves suggests a common trend in thermal behavior for the three alloys during the aging process. Initially, the thermal conductivity decreases gradually during the aging treatment, followed by an increase, then another decrease with ageing temperature, and finally a sharp increase in conductivity of the alloys beyond the aging temperature at 200°C. It is noteworthy that, in the alloys, the level of conductivity exhibits a reciprocal relationship with the material's hardness. This implies that as the hardness of an alloy increases, its conductivity tends to decrease, and vice versa. The initial decrease in conductivity is associated with the formation of the GP zone, while the subsequent increase is attributed to strain recovery from casting and the GP zone dissolution. The further decreases in conductivity with aging temperature are due to the formation of metastable phases in the alloys. The sharp increase in conductivity at the final stage is believed to be result from the dissolution of metastable phases and the coarsening of precipitates that had already formed in the matrix [35]. The presence of trace Ti in the alloy results in decreased conductivity, primarily due to the development of Ti tri-aluminide intermetallic compounds. This formation contributes to increased scattering of both electrons and phonons, alongside the distortion of the aluminum matrix's lattice structure, which ultimately reduces the thermal transport of electrons. Furthermore, the refinement of the grain structure contributes to the overall reduction in conductivity. The introduction of Zr further accelerates these effects by promoting the formation of Zr tri-aluminide intermetallics. Additionally, these two trace alloy additions delay the onset of certain phenomena, as these intermetallics exhibit significant stability against coarsening and the re-dissolution of precipitates [27].

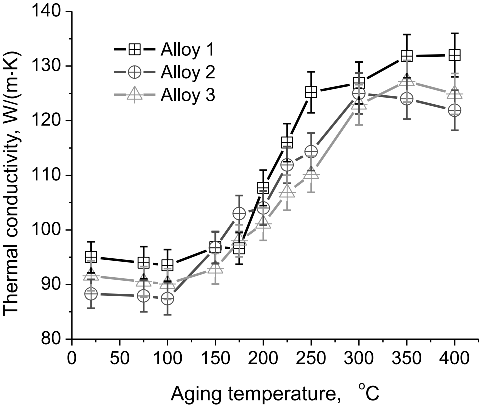

Fig. 3. Thermal conductivity curves resulting from the experimental alloys' 90-minute isochronal aging.

3.1.3. Artificial aging-isothermal aging. Figures 4 and 5 depict the variations in hardness observed in three experimental alloys subjected to isothermal aging at temperatures of 225°C and 250°C for varying durations, extending up to six hours. Initially, both aging conditions result in an increase in the alloys' hardness, attributed to the formation of high-density GP zones, which exhibits significant strengthening capabilities. However, as the aging duration increases, a decline in hardness is observed, primarily due to the dissolution of the GP zones. Following this dissolution, the precipitates undergo growth to attain a stable

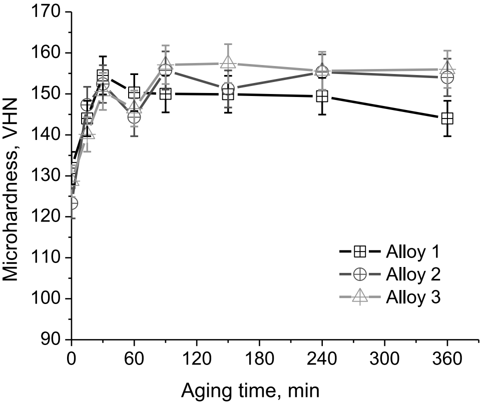

Fig. 4. Evolution of hardness in alloys subjected to isothermal aging at 225°C for a specified duration.

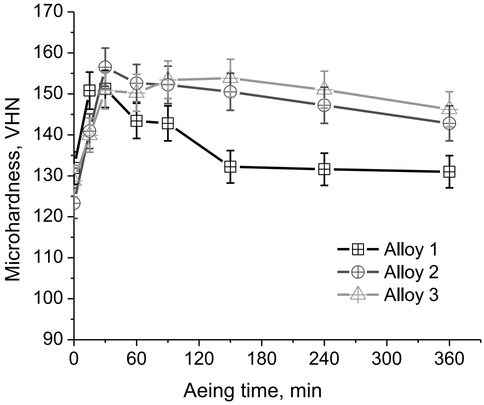

FIG. 5. Evolution of hardness in alloys subjected to isothermal aging at 250°C for a specified duration.

phase, leading to a relatively modest strengthening effect. Subsequent strengthening phenomena are linked to the presence of nanoscale metastable precipitates [36]. In the final stages of aging at elevated temperatures, a reduction in hardness occurs due to over-aging and the coarsening of precipitates.

The isothermal age hardening curves indicate that the alloy without trace additions reaches its peak hardness at a comparatively lower aging temperature and shorter duration than the other two alloys. The addition of Ti results in the formation of Al_3Ti, while Zr leads to the formation of Al_3Zr; both exhibit low solubility and diffusion coefficients within the aluminum matrix. These additions result in minimal lattice mismatch with the matrix, which effectively reduces the interfacial energy between the matrix and the precipitates. As a result, the precipitates show considerable resistance to coarsening within the matrix and possess improved thermal stability, attributed to their elevated melting points in comparison to the aluminum matrix [37].

The aging effect is notably more pronounced at elevated temperatures across all alloys. When comparing the impacts of exposure time and temperature, it is evident that temperature exerts a more substantial influence than exposure time. This observation suggests that the rate of diffusion is accelerated more by increased temperature than by extended time [2, 38]. Considering the combined effects of time and temperature, it can be inferred that optimal precipitation occurs after aging at 200°C for 90 min, where maximum hardness is attained.

The average thermal conductivity values for the three experimental alloys subjected to isothermal aging at temperatures of 225°C and 250°C are illustrated in Figs. 6 and 7. These figures reveal a consistent trend of increasing conductivity over the aging period. Notably, during the initial 150 minutes of aging, fluctuations in conductivity are observed. This variability can be attributed to

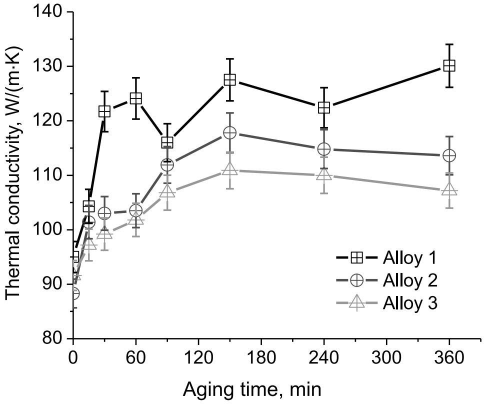

Fig. 6. Evolution of thermal conductivity in alloys subjected to isothermal aging at 225°C for a specified duration.

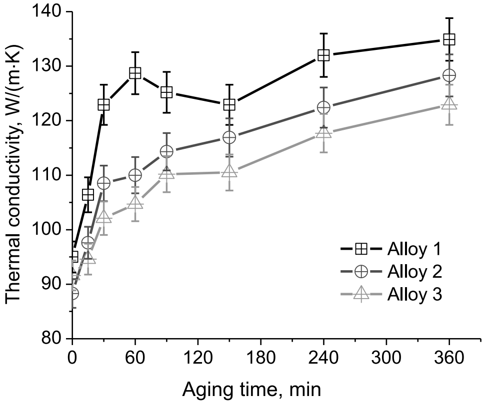

Fig. 7. Evolution of thermal conductivity in alloys subjected to isothermal aging at 250°C for a specified duration.

two interrelated factors: the formation of GP zones and various precipitates, which tend to reduce the alloys' conductivity, and the processes of stress relief and recovery, which enhance it. The cumulative effects of these phenomena are represented in the graphs. At longer aging times, the increase in conductivity is predominantly associated with precipitation and grain coarsening within the alloys. The presence of fine precipitates introduces defects that impede electron mobility, while coarser precipitates reduce overall efficiency, resulting in both lower and higher conductivity values. Furthermore, Alloy 3, which incorporates both Ti and Zr, exhibits the smallest increase in conductivity, followed by Alloy 2, which contains only Ti, compared to to the base Alloy 1. This observation highlights the influence of fine precipitates resulting from trace additions. As the aging temperature increases, diffusion processes are significantly accelerated, making the temperature's impact more pronounced than that of aging time. Consequently, the rate of conductivity enhancement is greater and occurs more rapidly at higher aging temperatures [24, 29].

3.2. Tensile properties

The investigation into the impact of trace additions on tensile testing at a strain rate of 10^{-3} 1/s was conducted for base Al-Si engine block alloy, alongside two additional alloys. Figures 8 and 9 illustrate the true stress and true strain outcomes derived from the tensile tests performed under peak-aged and over-aged conditions, specifically aged at 225°C for 90 min and at 250°C for 360 min, respectively. The true stress-strain curves for the base Alloy 1 show minimal variation when compared to the two trace-added alloys under peak-aged conditions (Fig. 8). Notably, the slope of the graph for the base alloy is comparatively steeper, despite exhibiting lower strength. This phenomenon can be explained through dislocation theory, which posits that precipitated particles serve as obstacles to dislocation movement [39, 40]. Consequently, this obstruction results in a deceleration of dislocation motion, leading to a reduction in slope and an enhancement in tensile strength. It is widely acknowledged that alloys in their peak-aged state achieve the highest concentration of fine dispersoid precipitates, thereby reinforcing the material. Therefore, no significant differences are detected among the alloys, with the exception of the grain-refining effects contributed by Ti and Zr.

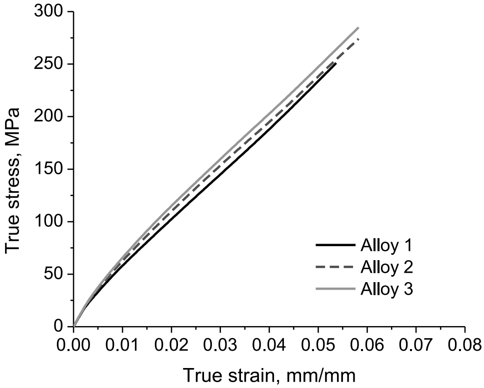

FIG. 8. True stress-true strain diagram of the experimental alloys in the peak-aged state.

The inclination of the stress-strain curves for all three alloys increases as they reach the over-aged state, which can be attributed to the phenomenon of precipitation coarsening within the alloys (Fig. 9). The coarsening precipitate loses its ability to impede dislocation movement as it grows in size. In contrast,

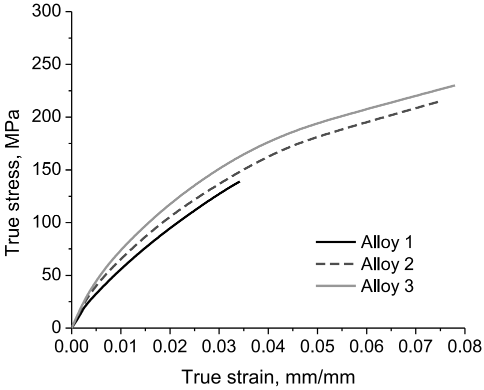

Fig. 9. True stress-true strain diagram of the experimental alloys in the over-aged state.

Alloy 2, which contains added trace Ti forms Al_3Ti trialuminide particles that are highly resistant to coarsening and re-dissolution. This leads to a more uniform distribution of dislocations and the pinning of grain boundaries, even after peak aging, resulting in a lower slop and higher strength. Alloy 3, which contains Ti and Zr additions, forms $Al_3(Ti, Zr)$ trialuminide particles that further enhance resistance to coarsening and re-dissolution, ultimately achieving the best performance. Notably, the elongation of the trace-added alloys also increases, likely due to morphological changes in long Si particles and other elements during rapid solidification [41].

The average ultimate tensile strength, along with the percentage elongation at break, obtained from the tensile tests, are taken into consideration to provide a clearer understanding of the results. It should be noted that the results pertaining to three alloys under aged, peak-aged, and over-aged conditions are presented in the bar charts in Figs. 10 and 11. In the absence of aging treatment,

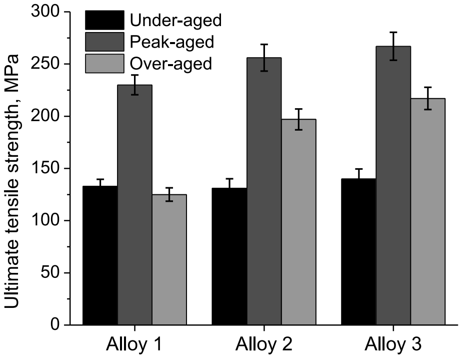

Fig. 10. Average ultimate tensile strength of the experimental alloys under different aging state.

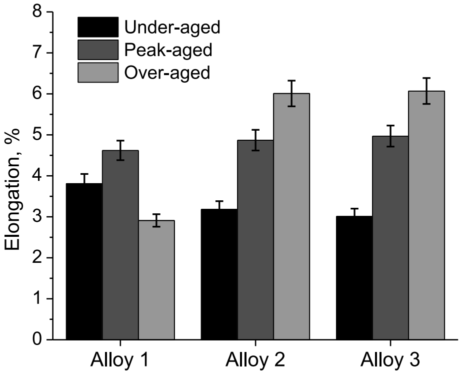

Fig. 11. Average percentage elongation of the experimental alloys under different aging state.

the alloys are classified asunder-aged, where the strength is comparatively low due to the alloying elements remaining in a solid solution state. During this initial phase, there are no additional advantages from trace additions, and the strength is compacted due to the morphological shift of brittle Si particles. Upon reaching the peak-aged condition, an enhancement in tensile strength is observed, attributed to the formation of various intermetallics as previously discussed; however, alloys with trace elements exhibit superior strength, mainly due to the grain-refining effects. The notable advantage in terms of reduced strength degradation is evident in the over-aged condition where the presence of Ti and Zr hinders precipitation coarsening and the movement of dislocations within the alloy structure. A similar scenario is observed with elongation percentages. In the under-aged condition, the addition of trace elements shows limited benefits. However, at the peak-aged condition, the grain-refining effect contributes to higher elongation, while in the over-aged condition, precipitation coarsening leads to significantly greater elongation percentages. Specifically, Ti plays a crucial role in refining the grain structure and morphological alterations by eliminating the brittle Si phases, resulting in elevated elongation percentages. Moreover, the addition of Zr further enhances these effects, ensuring a higher elongation percentage in the alloy [42, 43].

3.3. *Impact toughness properties*

Figure 12 provides a graphic representation of the impact toughness characteristics exhibited by the three experimental alloys. These alloys were subjected to a solution treatment process, followed by isochronal aging lasting for 90 min. The results show that as the aging temperature increases, the impact energy decreases. This phenomenon can be linked to the formation of GP zones,

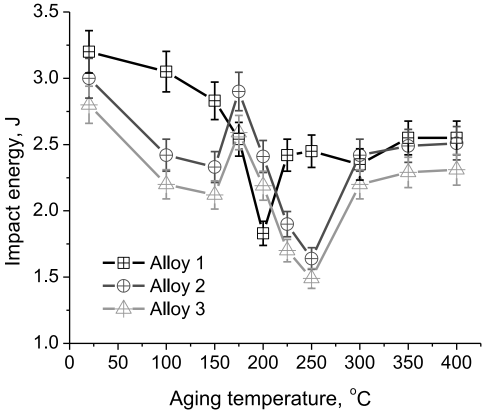

Fig. 12. The relationship between impact energy and aging temperature for alloys subjected to isochronal aging for 90 min.

which is subsequently followed by an increase in impact energy due to the dissolution of these zones. However, as the aging temperature continues to rise, a further decrease in impact energy is observed, associated with the emergence of metastable phases that enhance the matrix strength at the cost of ductility. The greatest reduction in absorbed energy occurs due to the precipitation of intermetallic phases in the peak-aged condition. Notably, there is a significant increase in impact energy from the peak-aged state to the over-aged condition, attributed to the softening of the microstructure at elevated aging temperatures [44]. Initially, alloys containing both Ti and Zr exhibit the lowest impact energy, followed by the alloy with only Ti. This is due to a higher volume fraction of alloying elements precipitating and diffusing from the solid solution to accumulate at the grain boundaries during casting. The grain refinement effect, along with the presence of these particles at the grain boundaries, contributes to brittle fracture [45]. It is important to note two aspects: first, during the dissolution stage of aging, the grain boundaries can absorb maximum strength, resulting in higher impact energy, and second, the trace-added alloys experience a delayed formation of precipitates that hinder alloy's performance.

3.4. Thermal analysis

The heating curve shown in Fig. 13 depicts the differential scanning calorimetry (DSC) analysis of three distinct alloys in their solution-treated state. Each alloy exhibits a total of five exothermic peaks, suggesting a commonality in the number of phase transformations taking place. Table 2 presents the peak temperatures along with the associated activation energies for the different alloys evaluated in this study. Notably, variations exist in the intensity and tempera-

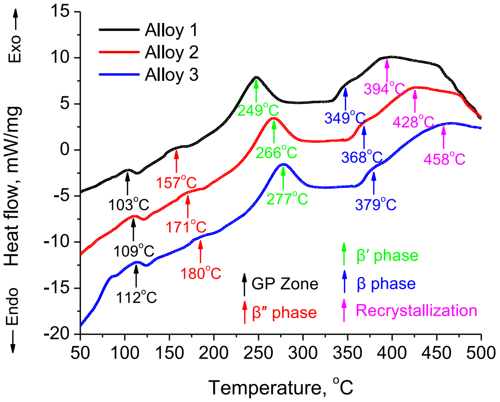

FIG. 13. Heating curve from DSC analysis for the three alloys subjected to solution treatment.

TABLE 2. Results of DSC study for alloys.

Alloy	Transformation	Peak temperature, °C	Activation energy, kJ/mol
Alloy 1	GP zone	103	65
	β'' phase	157	80
	β' phase	249	180
	β phase	349	201
	Recrystallization	394	135
Alloy 2	GP zone	109	71
	β'' phase	171	93
	β' phase	266	185
	β phase	368	205
	Recrystallization	428	158
Alloy 3	GP zone	112	74
	β'' phase	180	101
	β' phase	277	195
	β phase	379	211
	Recrystallization	458	176

ture at which these transformations occur, signifying differences in the specific phase transitions within each alloy. The sequence of exothermic peaks observed corresponds to the formation of GP zones, the β'' phase, the β' phase, the β phase, and finally, a broad peak representative of recrystallization. An interesting insight from this analysis is the hypothesis that the dissolution of prior phases is primarily driven by the need to initiate subsequent phases in the sequential phase transformation process [46, 47]. As shown in Fig. 13 and Table 2, for base Alloy 1, the formation of GP zones begins at 103°C, with an associated activation energy of 65 kJ/mol.

In contrast, Alloy 2, which contains Ti, exhibits GP zone formation at a higher temperature of 109°C with an activation energy of 71 kJ/mol. Furthermore, Alloy 3, which incorporates both Ti and Zr, shows GP zone formation at 112°C, with an activation energy of 74 kJ/mol. These values are comparable to the previously reported activation energy for the GP zones, which is 67 kJ/mol [46]. In a comparable manner, the activation energies for Alloy 1 are determined for the homogeneous β'' phase, the heterogeneous precipitation of β' phase, and then the stable equilibrium phase β as 80, 180, and 201 kJ/mol, respectively, at temperatures of 157°C, 249°C, and 349°C. In contrast, Alloy 2 exhibits activation energies of 93, 185, and 205 kJ/mol at corresponding temperatures of 171°C, 266°C, and 368°C. Alloy 3 shows activation energies of 101, 195, and 211 kJ/mol at temperatures of 180°C, 277°C, and 379°C. Previous studies have indicated a similar trend regarding the occurrence of these peaks [46]. Notably, in all instances, the addition of trace elements results in an increase in the activation energy required for each peak transition, which occurs at higher temperatures. This suggests that the incorporation of trace alloying elements significantly impedes the kinetics of recrystallization, primarily due to the formation of fine, coherent precipitates that generate substantial coherency strains, thereby obstructing dislocation movement. As a result, a greater amount of energy is required to elevate the activation energy to a higher threshold [47].

Finally, it is noteworthy that three specific alloys demonstrate a notable exothermic peak at distinctive temperatures of 394°C, 428°C, and 458°C, with corresponding activation energies for the crucial recrystallization phase measured at 135 kJ/mol, 158 kJ/mol, and 176 kJ/mol, respectively. Previously studies on the A356 alloy in its as-cast state report an activation energy of 127 kJ/mol for recrystallization [48]. While conventional wisdom suggests that 400°C is the optimal temperature for recrystallization initiation, empirical data reveals that the process actually commences at elevated temperatures for all the alloys studied. Moreover, it is important to note that the activation energy required for recrystallization in this specific scenario is considerably higher for both trace-added alloys in this study.

3.5. Optical microscopy

In Fig. 14, a detailed optical micrograph that highlights the differences among base Alloy 1, Alloy 2 infused with trace Ti, and Alloy 3 incorporating Ti and Zr is provided. These images showcase the impact of trace element additions across various aging treatments. The experimental automotive alloys undergo a series of thermal processes where they undergo solution treatment at 530°C for 2 h, followed by aging treatments at 225°C for 90 min to reach the peak-aged status, and at 250°C for 360 min to achieve an over-aged condition. During the

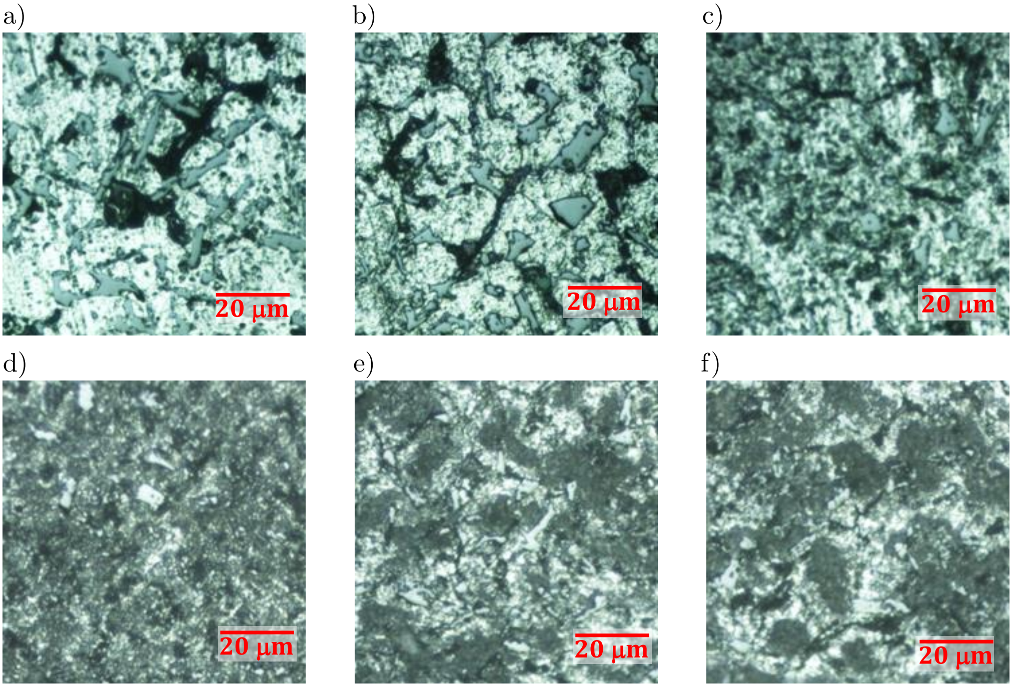

Fig. 14. Optical microstructure of solution-treated and aged at 225°C for 90 min: a) base Al-Si engine block Alloy 1, b) Ti-added Alloy 2, c) Ti and Zr-added Alloy 3, and aged at 250°C for 360 min: d) Alloy 1, e) Alloy 2, f) Alloy 3.

peak aging stage, the alloys maintain their grain orientation unchanged, but undergo stress relief and precipitation phenomena as a result of this specific heat treatment sequence. Each of the three alloys displays the characteristic dendritic structure, but with distinct differences in spacing. The microstructure of the base Alloy 1, an Al-Si automotive alloy, primarily consists of the aluminum α-phase, eutectic silicon, and assorted intermetallic compound particles (Fig. 14a). The introduction of trace Ti in Alloy 2 leads to a finer grain structure compared to the base Alloy 1, due to the grain refinement induced by Ti through the formation of Al_3Ti particles, simultaneously serving as nucleation sites during solidification (Fig. 14b). With the subsequent addition of Zr, further refinement occurs, resulting in the creation of additional Al_3Zr particles as well as combined Al_3(Ti, Zr) particles (Fig. 14c) [49, 50].

Upon aging at 250°C for 360 min, representing the over-aged condition, the microstructure of base Alloy 1 entirely recrystallizes, revealing equiaxed grains (Fig. 14d). Conversely, both Alloy 2 and Alloy 3, infused with trace elements, exhibit partial recrystallization of their microstructures, highlighting the grain evolution (Fig. 14e and Fig. 14f). The formation of numerous nanosized Al_3Ti

precipitates during solidification and aging remains crucial, as they form a coherent structure within the matrix. These precipitates act as effective barriers, hindering dislocation motion and delaying precipitation coarsening, pinning grain boundaries in the alloys. Consequently, they effectively impede the recrystallization process in the alloy system, contributing significantly to its overall stability and microstructural integrity [51]. The simultaneous incorporation of Ti and Zr elements can significantly increase the volume fraction of precipitates by promoting the formation of additional $L1_2$ $Al_3(Ti, Zr)$ dispersoids. The emergence of these $L1_2$ precipitates is linked to improved recrystallization resistance and an increased dislocation density, both of which play a crucial role in enhancing dislocation strengthening.

3.6. Scanning electron microscopy

Three distinct alloys were chosen for examination of the SEM microstructural changes following a 90-minute aging process at 225°C. Figure 15 shows the SEM images in conjunction with energy dispersive X-ray spectroscopy (EDX) analysis of these alloys. The microstructural analysis reveals that the predominant features include primary aluminum dendrites, eutectic silicon, and various intermetallic compounds such as Al_2Cu, Mg_2Si, Al_5FeSi, Al_8Mg_3FeS, Al_3CuNi, and Al_3Ni, all situated within the inter-dendritic regions of the α-Al matrix [52]. A significant presence of needle-like phases was observed at the grain boundaries, while smaller block-like phases were found precipitating within the α-Al grains of the base alloy (Fig. 15a).

The EDX analysis confirmed the composition, indicating a weight percentage of 2.15% Al, 97.27% Si, 0.15% Cu, 0.11% Mg, and 0.32% Ni. The SEM images illustrate the microstructure of the base alloy modified with Ti, revealing a relatively finer grain structure and morphological alterations in the eutectic silicon, attributed to titanium's role as a nucleating agent during alloy solidification (Fig. 15b). The energy dispersive spectroscopy (EDS) analysis of the titanium-modified alloy indicated a composition of 2.78% Al, 96.70% Si, 0.11% Ti, 0.02% Zr, 0.10% Cu, 0.08% Mg, and 0.21% Ni, demonstrating a drop in Si and a rise in Al compared to the base alloy. Figure 15c presents the microstructure of the alloy modified with both Ti and Zr. Compared to Fig. 15b, a further refinement is evident, characterized by a reduction in the size of the eutectic silicon and more pronounced morphological changes [53]. The EDS results corresponding to this SEM image reveal a composition of 9.73% Al, 89.65% Si, 0.10% Ti, 0.17% Zr, 0.11% Cu, 0.07% Mg, and 0.17% Ni, indicating the lowest silicon and the highest aluminum levels relative to the base alloy.

An investigation into the effects of trace amounts of Ti, as well as a combination of Zr, on the fracture morphology of engine block alloy has been conducted

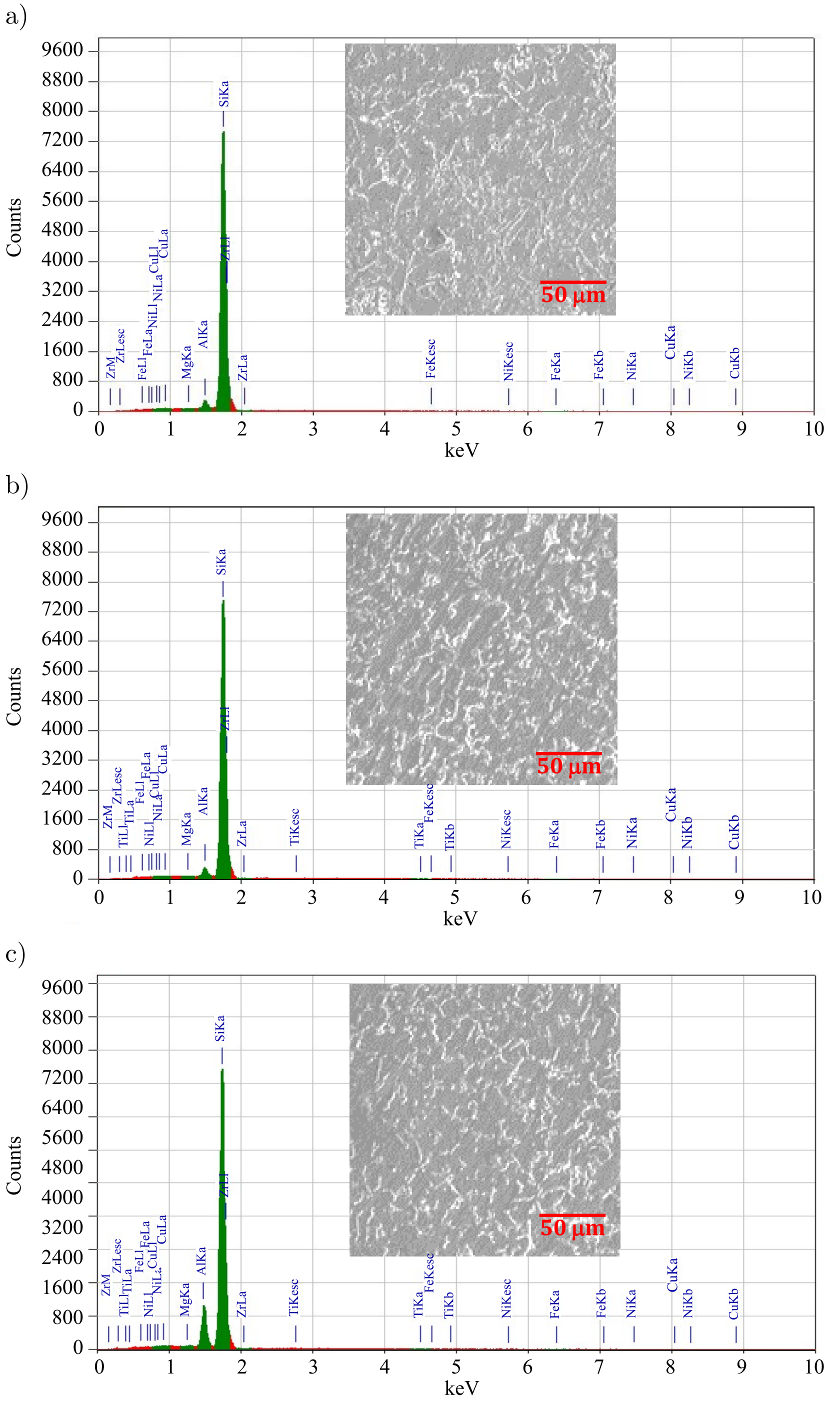

FIG. 15. SEM images with EDX analysis for: a) the engine block Alloy 1, b) Alloy 2 with added Ti, and c) Alloy 3 with both Ti and Zr at their peak-aged condition.

through SEM analysis, with the findings presented in Fig. 16. The specimens underwent a solution treatment, followed by aging for 90 min at 225°C, and were subsequently tensile tested with a strain rate set at 10^{-3} 1/s. Results suggest a clear disparity in the fracture behavior of the base engine block alloy, and alloys containing minor additional elements. The fracture surfaces of the engine block exhibit brittle fractures whereas the trace-added alloys show a combination of brittle and ductile fractures in the peak-aged condition. Alloy 1, the engine block, exhibits a cleavage pattern characterized by flat facets, which are indicative of the Al-Si eutectic zone [54, 55]. Within these flat regions, silicon platelets may separate from the aluminum matrix, leading to the formation of terraces with smooth facets. These features are likely attributed to the fracture of the brittle silicon phase crystals. In contrast, the micrographs of trace-added Alloy 2 and Alloy 3 reveal broken flat regions alongside other intermetallic compounds. The presence of grain refinement and additional intermetallic phases contributes to the reduced size of the flat surfaces observed [56]. Consequently, both trace-added alloys display finer flat surfaces, suggesting that the stress field associated with the addition of these elements disrupts the intermetallic phases due to their inferior deformation characteristics. Additionally, the dimensions of the dimples are reduced, while their quantity increases. This scenario demonstrates a greater degree of grain refinement for alloys with combined trace additions compared to those with only Ti added.

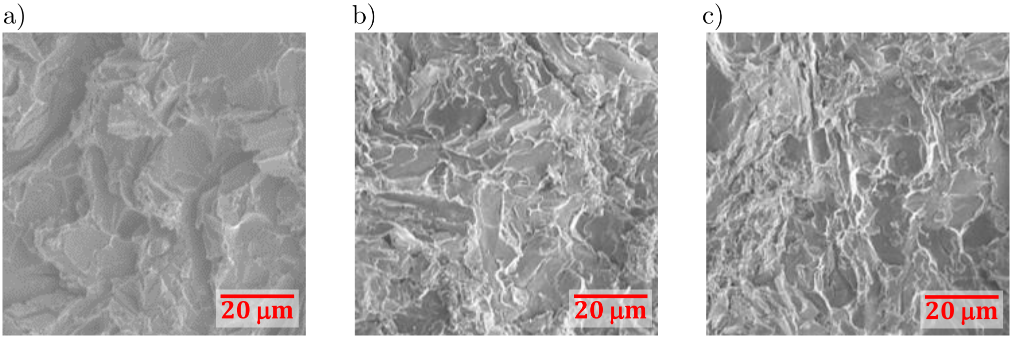

Fig. 16. Fracture surfaces investigated through SEM analysis in engine block Al-Si alloys: a) base Alloy 1, b) Ti-added Alloy 2, and c) both Ti and Zr-added Alloy 3.

4. Summary and conclusions

The experiment led to the following conclusions:

Incorporating trace amounts of Ti and Zr into Al-Si engine block alloy significantly affects the morphology and spatial distribution of eutectic silicon particles. Age-hardening reveals two maxima: the first due to the formation of GP-zones, and the second to the development of metastable particles. Notably, the incorporation of Ti into hypoeutectic Al-Si automotive alloys does not yield any observable age-hardening effect. Nevertheless, during aging, a comparatively lower degree of softening is recorded compared to the base alloy. This phenomenon is attributed to the formation of $L1_2$-ordered Al_3Ti particles during solidification and aging, which impede dislocation movement within the alloy matrix. Consequently, this results in a delay of various thermal processes, including the formation of GP zones, the dissolution of certain phases, and recrystallization. Furthermore, the addition of Zr facilitates the formation of additional Al_3Zr as well as $Al_3(Ti, Zr)$ particles, thereby accelerating these processes. The optimal hardness for the alloys achieved through aging at approximately 225°C for 90 min.

The thermal conductivity of the engine block alloy decreases with the incorporation of Ti and Zr, as these elements contribute to the formation of a tri-aluminide compound. This process also leads to grain refinement, which obstructs the movement of electrons and phonons. However, during the aging process, the thermal conductivity continues to decrease due to the formation of precipitates. Conversely, at elevated temperatures, the conductivity increases as a result of internal stress relief, the dissolution of metastable phases, and the coarsening of precipitates within the alloy.

In an Al-Si engine block alloy, adding trace elements like Ti and Zr does not significantly increase tensile strength but helps slow down strength degradation. As the alloy becomes over-aged, its strength decreases due to the coarsening of intermetallic compounds. However, trace elements help maintaining strength at high aging temperatures by promoting the formation of Al_3Ti and Al_3Zr precipitates, which resist coarsening and enhance thermal stability. Additionally, these trace additions improve the alloy's elongation properties through morphological changes.

The DSC analysis further validates the presence of distinct peaks associated with the development of GP zones, as well as the β'', β', β, and recrystallization phases, which occur in alloys with trace additions at elevated temperatures and higher activation energies. The presence of trace alloying elements markedly hinders the recrystallization kinetics, primarily due to the formation of fine, coherent precipitates that introduce significant coherency strains, which in turn hinder dislocation movement. Consequently, an increased amount of energy is required to raise the activation energy to a higher level.

The base alloy exhibits a coarse dendritic morphology, while the Ti-modified alloy shows a dendritic structure that is partially formed through the heterogeneous nucleation of Al_3Ti particles. The subsequent addition of Zr plays a crucial role in further refining the microstructure, resulting in a fine equiaxed structure attributed to an increased level of heterogeneous nucleation of $Al_3(Ti, Zr)$. After aging at 250°C for 360 min, the base alloy undergoes nearly complete recrystallization; in contrast, the alloys with trace elements do not demonstrate this behavior. This phenomenon is mainly due to the precipitates acting as effective barriers that impede dislocation movement and pin the grain boundaries within the alloys.

In terms of fracture behavior, the base alloy displays brittle fracture, while the trace-added alloys exhibit both brittle and ductile fracture modes. These differences likely linked to the fracture of brittle Si-phase crystals in the base alloy. Conversely, the trace-added alloys demonstrate fractured flat regions in conjunction with various intermetallic compounds. The observed reduction in the size of these flat surfaces can be attributed to the influences of grain modification through refinement and the presence of additional intermetallic phases, which enhance the material's ability to absorb energy and improve its ductility.

Acknowledgments

The author would like expresses gratitude to the esteemed Treasurer for their substantial support and motivation, which has greatly contributed to the advancement of research activities at IUBAT, Dhaka.

References

1. Hernandez F.C.R., Ramírez J.M.H., Mackay R., *Al-Si Alloys: Automotive, Aeronautical, and Aerospace Applications*, 2nd ed., Springer, London, UK, 2017, https://doi.org/10.1007/978-3-319-58380-8.

2. Razin A.A., Ahammed D.S-S., Khan A.A., Kaiser M.S., Thermophysical properties of hypoeutectic, eutectic and hypereutectic Al-Si automotive alloys under ageing treatment, *Journal of Chemical Technology and Metallurgy*, **59**(3): 673–682, 2024, https://doi.org/10.59957/jctm.v59.i3.2024.22.

3. Torres R., Esparza J., Velasco E., Garcia-Luna S., Colas R., Characterisation of an aluminium engine block, *International Journal of Microstructure and Materials Properties*, **1**(2): 129–138, 2006, https://doi.org/10.1504/IJMMP.2006.010621.

4. Hoag K., Dondlinger B., *Vehicular Engine Design*, 2nd ed., Springer, London, UK, 2016.

5. Callegari B., Lima T.N., Coelho R.S., The influence of alloying elements on the microstructure and properties of Al-Si-based casting alloys: A review, *Metals*, **13**(7): 1174, 2023, https://doi.org/10.3390/met13071174.

6. Kaiser M.S., Khan A.A., Sharma S.D., Nur M.A., Investigation on electrochemical corrosion behavior of eutectic Al-Si automotive alloy in 0.2 M HCl, NaOH and NaCl environments, *Journal of Chemical Technology and Metallurgy*, **58**(5): 969–980, 2023.

7. Razin A.A., Ahammed D.S., Nur M.A., Kaiser M.S., Role of Si on machined surfaces of Al-based automotive alloys under varying machining parameters, *Journal of Mechanical and Energy Engineering*, **6**(1): 43–52, 2022, https://doi.org/10.30464/jmee.2021.6.1.43.

8. Ervina Efzan M.N., Kong H.J., Kok C.K., Review: effect of alloying element on Al-Si alloys, *Advanced Materials Research*, **845**: 355–359, 2013, https://doi.org/10.4028/www.scientific.net/amr.845.355.
9. Kaiser M.S., Sabbir S.H., Soumo M.R., Kabir M.S., Nur M.A., Heat treatment effect on the physical and mechanical properties of Fe, Ni and Cr added hyper-eutectic Al-Si automotive alloy, *Journal of Chemical Technology and Metallurgy*, **55**(2): 409–416, 2020.
10. Toschi S., Optimization of A354 Al-Si-Cu-Mg alloy heat treatment: effect on microstructure, hardness, and tensile properties of peak aged and overaged alloy, *Metals*, **8**(11): 961, 2018, https://doi.org/10.3390/met8110961.
11. Mao H., Bai X., Song F., Song Y., Jia Z., Xu H., Wang Y., Effect of Cd on mechanical properties of Al-Si-Cu-Mg alloys under different multi-stage solution heat treatment, *Materials*, **15**(15): 5101, 2022, https://doi.org/10.3390/ma15155101.
12. Mohamed A.M.A., Samuel F.H., A review on the heat treatment of Al-Si-Cu/Mg casting alloys, [in:] *Heat Treatment: Conventional and Novel Applications*, Czerwinski F. [Ed.], Ch. 4, IntechOpen, London, UK, 2012, https://doi.org/10.5772/50282.
13. Zuo L., Ye B., Feng J., Zhang H., Kong X., Jiang H., Effect of ε-Al_3Ni phase on mechanical properties of Al-Si-Cu-Mg-Ni alloys at elevated temperature, *Materials Science and Engineering: A*, **772**: 138794, 2020, https://doi.org/10.1016/j.msea.2019.138794.
14. Cho Y.H., Kim H.W., Lee J.M., Kim M.S., A new approach to the design of a low Si-added Al–Si casting alloy for optimising thermal conductivity and fluidity, *Journal of Materials Science*, **50**(22): 7271–7281, 2015, https://doi.org/10.1007/s10853-015-9282-8.
15. Cho Y.H., Joo D.H., Kim C.H., Lee H.C., The effect of alloy addition on the high temperature properties of over-aged Al-Si(CuNiMg) cast alloys, *Materials Science Forum*, **519–521**: 461–466, 2006, https://doi.org/10.4028/www.scientific.net/msf.519-521.461.
16. Gholizadeh R., Shabestari S.G., Investigation of the effects of Ni, Fe, and Mn on the formation of complex intermetallic compounds in Al-Si-Cu-Mg-Ni alloys, *Metallurgical and Materials Transactions A*, **42**(11): 3447–3458, 2011, https://doi.org/10.1007/s11661-011-0764-2.
17. Liu Y., Luo L., Han C., Ou L., Wang J., Liu C., Effect of Fe, Si and cooling rate on the formation of Fe- and Mn-rich intermetallics in Al-5Mg-0.8Mn alloy, *Journal of Materials Science & Technology*, **32**(4): 305–312, 2016, https://doi.org/10.1016/j.jmst.2015.10.010.
18. Zhang J.-Ch., Ding D.-Y., Zhang W.-L., Kang S.-H., Xu X.-L, Gao Y.-J, Chen G.-Z., Chen W.-G., You X.-H., Effect of Zr addition on microstructure and properties of Al–Mn–Si–Zn-based alloy, *Transactions of Nonferrous Metals Society of China*, **24**(12): 3872–3878, 2014, https://doi.org/10.1016/S1003-6326(14)63545-7.
19. Hideo Y., Yoshio B., The role of zirconium to improve strength and stress-corrosion resistance of Al–Zn–Mg and A–Zn–Mg–Cu alloys, *Transactions of the Japan Institute of Metals*, **23**(10): 620–630, 1982, https://doi.org/10.2320/matertrans1960.23.620.
20. Kaiser M.S., Kurny A.S.W., Effect of scandium on the grain refining and ageing behaviour of cast Al-Si-Mg alloy, *Iranian Journal of Materials Sciences and Engineering*, **8**(4): 1–8, 2011.
21. Chen J., Wen F., Liu C., Li W., Zhou Q., Zhu W., Zhang Y., Guan R., The microstructure and property of Al–Si alloy improved by the Sc-microalloying and Y_2O_3 nano-particles, *Science and Technology of Advanced Materials*, **22**(1): 205–217, 2021, https://doi.org/10.1080/14686996.2021.1891841.

22. Chen Z., Yan K., Grain refinement of commercially pure aluminum with addition of Ti and Zr elements based on crystallography orientation, *Scientific Reports*, **10**(1): 16591, 2020, https://doi.org/10.1038/s41598-020-73799-2.

23. Zhao Z., Li D., Yan X., Chen Y., Jia Z., Zhang D., Han M., Wang X., Liu G., Liu X., Liu S., Insights into the dual effects of Ti on the grain refinement and mechanical properties of hypoeutectic Al–Si alloys, *Journal of Materials Science & Technology*, **189**: 44–59, 2024, https://doi.org/10.1016/j.jmst.2023.12.014.

24. Chester G.V., Thellung A., The law of Wiedemann and Franz, *Proceedings of the Physical Society*, **77**(5): 1005-1013, 1961, https://doi.org/10.1088/0370-1328/77/5/309.

25. Guo M.X., Zhang Y.D., Li G.J., Jin S.B., Sha G., Zhang J.S., Zhuang L.Z., Lavernia E.J., Solute clustering in Al-Mg-Si-Cu-(Zn) alloys during aging, *Journal of Alloys and Compounds*, **774**: 347–363, 2019, https://doi.org/10.1016/j.jallcom.2018.09.309.

26. Spigarelli S., Cabibbo M., Evangelista E., Bidulská J., A study of the hot formability of an Al-Cu-Mg-Zr alloy, *Journal of Materials Science*, **38**: 81–88, 2003, https://doi.org/10.1023/A:1021161715742.

27. Wang Z., Pu Q., Li Y., Xia P., Geng J., Li X., Wang M., Chen D., Wang H., Microstructures and mechanical properties of Al-Zn-Mg-Cu alloy with the combined addition of Ti and Zr, *Journal of Materials Research and Technology*, **22**: 747–761, 2023, https://doi.org/10.1016/j.jmrt.2022.11.106.

28. Ding L., Jia Z., Zhang Z., Sanders R.E., Liu Q., Yang G., The natural aging and precipitation hardening behaviour of Al-Mg-Si-Cu alloys with different Mg/Si ratios and Cu additions, *Materials Science and Engineering: A*, **627**: 119–126, 2015, https://doi.org/10.1016/j.msea.2014.12.086.

29. Ghassemali E., Riestra M., Bogdanoff T., Kumar B.S., Seifeddine S., Hall-Petch equation in a hypoeutectic Al-Si cast alloy: Grain size vs. secondary dendrite arm spacing, *Procedia Engineering*, **207**: 19–24, 2017, https://doi.org/10.1016/j.proeng.2017.10.731.

30. Xiao L., Yu H., Qin Y., Liu G., Peng Z., Tu X., Su H., Xiao Y., Zhong Q., Wang S., Cai Z., Zhao X., Microstructure and mechanical properties of cast Al-Si-Cu-Mg-Ni-Cr alloys: Effects of time and temperature on two-stage solution treatment and ageing, *Materials*, **16**(7): 2675, 2023, https://doi.org/10.3390/ma16072675.

31. Gao T., Zhang Y., Liu X., Influence of trace Ti on the microstructure, age hardening behavior and mechanical properties of an Al-Zn-Mg-Cu-Zr alloy, *Materials Science and Engineering: A*, **598**: 293–298, 2014, https://doi.org/10.1016/j.msea.2014.01.062.

32. Lee H.M., Lee J., Lee Z.-H., Lattice misfit variation of Al_3(Ti, V, Zr) in Al-Ti-V-Zr alloys, *Scripta Metallurgica et Materialia*, **25**(3): 517–520, 1991, https://doi.org/10.1016/0956-716X(91)90082-C.

33. Knipling K.E., Dunand D.C., Seidman D.N., Precipitation evolution in Al-Zr and Al-Zr-Ti alloys during aging at 450–600°C, *Acta Materialia*, **56**(6): 1182–1195, 2008, https://doi.org/10.1016/j.actamat.2007.11.011.

34. Fan S., Guo X., Jiang Q., Li Z., Ma J, Microstructure evolution and mechanical properties of Ti and Zr micro-alloyed Al-Cu alloy fabricated by wire + arc additive manufacturing, *The Journal of the Minerals, Metals & Materials Society (TMS)*, **75**(10): 4115–4127, 2023, https://doi.org/10.1007/s11837-023-05900-9.

35. Kaiser M.S., Effect of trace impurities on the thermoelectric properties of commercially pure aluminum, *Materials Physics and Mechanics*, **47**(4): 582–591, 2021, https://doi.org/10.18149/MPM.4742021_5.

36. Sjölander E., Seifeddine S., The heat treatment of Al-Si-Cu-Mg casting alloys, *Journal of Materials Processing Technology*, **210**(10): 1249–1259, 2010, https://doi.org/10.1016/j.jmatprotec.2010.03.020.

37. Kaiser M.S., Effect of solution treatment on the age-hardening behavior of Al-12Si-1Mg-1Cu piston alloy with trace-Zr addition, *Journal of Casting and Materials Engineering*, **2**(2): 30–37, 2018, https://doi.org/10.7494/jcme.2018.2.2.30.

38. Kumar R.N., Prabhu T.R., Siddaraju C., Effect of thermal exposure on mechanical properties hypo eutectic aerospace grade aluminium-silicon alloy, *IOP Conference Series: Materials Science and Engineering*, **149**: 012047, 2016, https://doi.org/10.1088/1757-899X/149/1/012047.

39. Shaha S.K., Czerwinski F., Chen D.L., Kasprzak W., Dislocation slip distance during compression of Al–Si–Cu–Mg alloy with additions of Ti–Zr–V, *Materials Science and Technology*, **31**(1): 63–72, 2015, https://doi.org/10.1179/1743284714Y.0000000606.

40. Pio L.Y., Effect of T6 heat treatment on the mechanical properties of gravity die cast A356 aluminium alloy, *Journal of Applied Sciences*, **11**(11): 2048–2052, 2011, https://doi.org/10.3923/jas.2011.2048.2052.

41. Kim J.-H., Jeun J.-H., Chun H.-J., Lee Y.-R., Yoo J.-T., Yoon J.-H., Lee H.-S., Effect of precipitates on mechanical properties of AA2195, *Journal of Alloys and Compounds*, **669**: 187–198, 2016, https://doi.org/10.1016/j.jallcom.2016.01.229.

42. Shoummo M.R., Khan A.A., Kaiser M.S., True stress-strain behavior of Al-based cast automotive alloy under different ageing condition and the effect of trace Zr, *Journal of Mechanical Engineering Science and Technology*, **6**(2): 95–106, 2022, https://doi.org/10.17977/um016v6i22022p095.

43. Huda Z., *Mechanical Behavior of Materials, Fundamentals, Analysis, and Calculations, Mechanical Engineering Series*, Springer Cham, Switzerland, 2021, https://doi.org/10.1007/978-3-030-84927-6.

44. Ma A., Saito N., Shigematsu I., Suzuki K., Takagi M., Nishida Y., Iwata H., Imura T., Effect of heat treatment on impact toughness of aluminum silicon eutectic alloy processed by rotary-die equal-channel angular pressing, *Materials Transactions*, **45**(2): 399–402, 2004, https://doi.org/10.2320/matertrans.45.399.

45. Waheed A., Lorimer G.W., Pinning of subgrain boundaries by Al_3Zr dispersoids during annealing in Al-Li commercial alloys, *Journal of Materials Science Letters*, **16**(20): 1643–1646, 1997, https://doi.org/10.1023/A:1018557510550.

46. Hamdi I., Boumerzoug Z., Chabane F., Study of precipitation kinetics of an Al-Mg-Si alloy using differential scanning calorimetry, *Acta Metallurgica Slovaca*, **23**(2): 155–160, 2017, https://doi.org/10.12776/ams.v23i2.908.

47. Ludwig T.H., Schaffer P.L., Arnberg L., Influence of some trace elements on solidification path and microstructure of Al-Si foundry alloys, *Metallurgical and Materials Transactions A*, **44**(8): 3783–3796, 2013, https://doi.org/10.1007/s11661-013-1694-y.

48. Chaudhury S.K., Warke V., Shankar S., Apelian D., Localized recrystallization in cast Al-Si-Mg alloy during solution heat treatment: dilatometric and calorimetric studies,

Metallurgical and Materials Transactions A, **42**(10): 3160–3169, 2011, https://doi.org/10.1007/s11661-011-0716-x.

49. Feng J., Ye B., Zuo L., Qi R., Wang Q., Jiang H., Huang R., Ding W., Yao J., Wang C., Effects of Zr, Ti and Sc additions on the microstructure and mechanical properties of Al-0.4Cu-0.14Si-0.05Mg-0.2Fe alloys, *Journal of Materials Science & Technology*, **34**(12): 2316–2324, 2018, https://doi.org/10.1016/j.jmst.2018.05.011.

50. Knipling K.E., Dunand D.C., Seidman D.N., Precipitation evolution in Al–Zr and Al–Zr–Ti alloys during isothermal aging at 375–425°C, *Acta Materialia*, **56**(1): 114–127, 2008, https://doi.org/10.1016/j.actamat.2007.09.004.

51. Lee S.-H., Jung J.-G., Baik S-.I., Park S.-H., Kim M.-S., Lee Y.-K., Euh K., Effects of Ti addition on the microstructure and mechanical properties of Al-Zn-Mg-Cu-Zr alloy, *Materials Science and Engineering: A*, **801**: 140437, 2021, https://doi.org/10.1016/j.msea.2020.140437.

52. Farkoosh A.R., Javidani M., Hoseini M., Larouche D., Pekguleryuz M., Phase formation in as-solidified and heat-treated Al–Si–Cu–Mg–Ni alloys: thermodynamic assessment and experimental investigation for alloy design, *Journal of Alloys and Compounds*, **551**: 596–606, 2013, https://doi.org/10.1016/j.jallcom.2012.10.182.

53. Kasprzak W., Amirkhiz B.S., Niewczas M., Structure and properties of cast Al–Si based alloy with Zr–V–Ti additions and its evaluation of high temperature performance, *Journal of Alloys and Compounds*, **595**: 67–79, 2014, https://doi.org/10.1016/j.jallcom.2013.11.209.

54. Meng Y., Zhang H., Li X., Zhou X., Mo H., Wang L., Fan J., Tensile fracture behavior of 2A14 aluminum alloy produced by extrusion process, *Metals*, **12**(2): 184, 2022, https://doi.org/10.3390/met12020184.

55. Lados D.A., Apelian D., Major J.F., Fatigue crack growth mechanisms at the microstructure scale in Al-Si-Mg cast alloys: mechanisms in regions II and III, *Metallurgical and Materials Transactions A*, **37**(8): 2405–2418, 2006, https://doi.org/10.1007/BF02586215.

56. Kaiser M.S., Solution treatment effect on tensile, impact and fracture behaviour of trace Zr added Al–12Si–1Mg–1Cu piston alloy, *Journal of the Institution of Engineers (India): Series D*, **99**(1): 109–114, 2018, https://doi.org/10.1007/s40033-017-0140-5.

Received August 26, 2024; accepted version December 2, 2024.
Online first February 18, 2025.